Fluorogenic aptamers resolve the flexibility of RNA junctions using orientation-dependent FRET

SUNNY C.Y. JENG,[1,4] ROBERT J. TRACHMAN III,[2,4] FLORIAN WEISSENBOECK,[1] LYNDA TRUONG,[2] KATIE A. LINK,[2] METTE D.E. JEPSEN,[3] JAY R. KNUTSON,[2] EBBE S. ANDERSEN,[3] ADRIAN R. FERRÉ-D'AMARÉ,[2] and PETER J. UNRAU[1]

[1]Department of Molecular Biology and Biochemistry, Simon Fraser University, Burnaby, British Columbia, Canada V5A 1S6
[2]Biochemistry and Biophysics Center, National Heart, Lung, and Blood Institute, Bethesda, Maryland 20892-8012, USA
[3]Interdisciplinary Nanoscience Center, Aarhus University, 8000 Aarhus C, Denmark

ABSTRACT

To further understand the transcriptome, new tools capable of measuring folding, interactions, and localization of RNA are needed. Although Förster resonance energy transfer (FRET) is an angle- and distance-dependent phenomenon, the majority of FRET measurements have been used to report distances, by assuming rotationally averaged donor–acceptor pairs. Angle-dependent FRET measurements have proven challenging for nucleic acids due to the difficulties in incorporating fluorophores rigidly into local substructures in a biocompatible manner. Fluorescence turn-on RNA aptamers are genetically encodable tags that appear to rigidly confine their cognate fluorophores, and thus have the potential to report angular-resolved FRET. Here, we use the fluorescent aptamers Broccoli and Mango-III as donor and acceptor, respectively, to measure the angular dependence of FRET. Joining the two fluorescent aptamers by a helix of variable length allowed systematic rotation of the acceptor fluorophore relative to the donor. FRET oscillated in a sinusoidal manner as a function of helix length, consistent with simulated data generated from models of oriented fluorophores separated by an inflexible helix. Analysis of the orientation dependence of FRET allowed us to demonstrate structural rigidification of the NiCo riboswitch upon transition metal-ion binding. This application of fluorescence turn-on aptamers opens the way to improved structural interpretation of ensemble and single-molecule FRET measurements of RNA.

Keywords: RNA; fluorescent aptamer; FRET; riboswitch; helical junction; G-quadruplex

INTRODUCTION

All kingdoms of life possess numerous structured RNAs that are essential for proper cellular physiology. While many chemical tools have been developed to observe and measure protein function, analogous systems are often lacking for nucleic acids. Foremost, genetically encodable fluorescent markers revolutionized proteomics, enabling the measurements of localization, folding, and interactions (Rodriguez et al. 2017). Further development of fluorescent tools to measure RNA folding, dynamics, and colocalization are required to keep pace with the ever-expanding field of RNA biology (Schmidt et al. 2020).

Förster resonance energy transfer (FRET) between organic fluorophores has long been understood to be orientation- and distance-dependent when analyzed in the dipole–dipole Förster coupling model (Clegg 1992). Fluorophore rotation is difficult to prevent in solution; therefore, the vast majority of FRET studies have disregarded angular information and used FRET measurements as a type of "molecular ruler" (Stryer and Haugland 1967) to measure changes in molecular conformation or assembly (Heyduk 2002). Observing angular-dependent changes in FRET is significantly more challenging due to the difficulty of rigidly orienting both the donor and acceptor fluorophores within macromolecule(s).

Several synthetic strategies have been attempted to resolve angular information from FRET measurements. In vitro nucleic acid synthesis has allowed the attachment of fluorescein/rhodamine (Gohlke et al. 1994), Cy3/Cy5 (Iqbal et al. 2008a; Fessl and Lilley 2013) and pyrene/perylene (Kashida et al. 2017) FRET pairs to DNA or RNA. However, these approaches provide only transient fluorophore localization, due to low stacking propensity, and therefore suffer

[4]These authors contributed equally to this work.

Corresponding authors: robert.trachman@nih.gov, punrau@sfu.ca

Article is online at http://www.rnajournal.org/cgi/doi/10.1261/rna.078220.120.

from significant rotational averaging (Sanborn et al. 2007; Iqbal et al. 2008b; Spiriti et al. 2011). To overcome the limitations imposed by rotational averaging, a stilbene/perylene (Lewis et al. 2005) FRET pair along with fluorescent cytosine analogs have been used to generate sensitive orientation-dependent FRET (Börjesson et al. 2009). Additionally, a Cy3/Cy5 FRET pair was introduced internally to a DNA helix and found to be sensitive to backbone motions (Lee et al. 2014). Nevertheless, all of these strategies preclude the study of biologically transcribed RNA either in vitro or in vivo.

Fluorogenic aptamers, RNAs that bind and enhance fluorescence of otherwise dark molecules, are promising chemical tools for studying interactions (Lacerda et al. 2017), folding (Kellenberger et al. 2015), and localization (Strack et al. 2013) of RNA. Several fluorogenic RNA aptamers bind and appear to rigidly orient fluorophores in a biologically compatible manner. Recently, it was shown that a 4-cyanoindole/Chili-DMHBI$^+$ (Steinmetzger et al. 2020) FRET pair can be used to map the binding site of a fluorescent aptamer. By incorporating the fluorogenic aptamer FRET (apta-FRET) pairs, Mango-I (Dolgosheina et al. 2014), Spinach (Paige et al. 2011), and Broccoli (Filonov et al. 2014), or Mango-IV (Autour et al. 2018) and *i*Spinach (Autour et al. 2016), into self-assembling RNA structures, it was recently shown that apta-FRET is indeed possible (Jepsen et al. 2018; Trachman et al. 2020). However, the crystal structures of Mango-I (Trachman et al. 2017a) and Mango-IV (Trachman et al. 2020) suggest considerable flexibility at the junction of the fluorophore-binding pocket and variable helix; therefore, these aptamers would be predicted to exhibit rotational averaging. In contrast, the crystal structures of Mango-III (Trachman et al. 2019a,b), and Spinach (Warner et al. 2014) indicate that both fluorogen-binding aptamer cores are rigidly connected to external helical elements. Thus, rotational averaging would not be expected from this apta-FRET pair.

To determine the integrity of complex RNA junctions, we sought to develop an orientation-dependent FRET system using apta-FRET pairs. The combination of Mango-III and Broccoli (Filonov et al. 2014) enables robust orientation-dependent FRET, while the Mango-I/Broccoli chimeras are rotationally averaged. The fluorophores of Mango-III and Broccoli are therefore rigidly positioned relative to the connecting helix while the helical junction of Mango-I is flexible. The Mango-III/Broccoli chimeras are in agreement with the dipole–dipole coupling approximation, thus supporting the hypothesis that the fluorophore dipole vectors are positioned nearly perpendicular to, and rigid along, the helical axis separating the two aptamers. Using the rigidly connected Mango-III and Broccoli FRET pairs, the flexibility of the NiCo riboswitch (Furukawa et al. 2015) four-way junction was studied. By altering the distance and rotation between apta-FRET pairs, we observe that the unfolded, apoNiCo riboswitch lacks defined structure while the folded, Co^{2+} bound, NiCo riboswitch is surprisingly rigid. These data demonstrate the ability to resolve the orientation dependence of FRET using fluorescent aptamers and provide the foundation for improving structural interpretation of ensemble and single-molecule FRET measurements.

Theory and background

In the dipole–dipole approximation, which has some notable limitations at short distances (Muñoz-Losa et al. 2009), E_{FRET} (the quantum efficiency of energy transfer between a donor and acceptor fluorophore) is related to the sixth power of the distance between the two molecules, and is given by:

$$E_{FRET} = \frac{1}{1 + \left(\frac{R}{R_0}\right)^6}. \quad (1)$$

Here R is the distance between the two fluorophores and the Förster radius (R_0) is the distance where E_{FRET} is 50%. Importantly R_0^6 is directly proportional to the orientation factor κ^2 defined by Equation 2 (Scheme 1):

$$\kappa^2 = (\hat{d} \cdot \hat{a} \ - 3(\hat{d} \cdot \hat{R})(\hat{a} \cdot \hat{R}))^2. \quad (2)$$

Here $\hat{d}$ is a unit vector representing the donor excitation dipole orientation and $\hat{a}$ is a unit vector representing the acceptor dipole orientation, both of which can point in any given direction (see Scheme 1). $\vec{R}$ is the vector from the donor fluorophore (green circle) to the acceptor fluorophore (red circle) and $\hat{R}$ is the corresponding unit vector. The Förster radius is given by:

$$R_0^6 = \alpha \phi_D \kappa^2 \quad (3)$$

where α is determined from the following parameters: J_{DA} the spectral overlap between the donor and acceptor and η the index of refraction of the medium between the two dipoles (Börjesson et al. 2009). Importantly, in the dipole approximation the parameters α and ϕ_D are constants that can be related to the properties of each fluorophore in isolation. Thus, and discounting changes in permittivity of the space (proportional to η^2) between the two dipoles, E_{FRET} depends on only the distance R between the dipoles, and the orientation factor κ^2 as defined by Equation 2. While the Förster radius, as defined by Equation 3, is traditionally

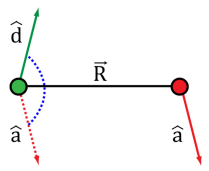

SCHEME 1. Diagram of fluorophore angles, distances and vectors defined in Equation 2.

used, it complicates FRET analysis as it is not directly related to the experimental observables seen in a typical (time-independent) FRET experiment. Here, we define a more experimentally accessible characteristic radius, which can be simply related to standard FRET donor and acceptor peak areas observed using a fluorometer:

$$R_0'^6 = \alpha\phi_A\kappa^2 \tag{4}$$

where ϕ_A is the quantum yield of the acceptor fluorophore in isolation. The experimental difference between these two measures can be negligible, for example when the donor and acceptor quantum yields are within a factor of three of each other ($1/3 < \phi_D/\phi_A < 3$), then the error between R_0 and R'_0 is <20% (i.e., $0.83 < R_0/R'_0 < 1.20$), and, if needed, can be easily corrected for via Equations 3 and 4. The advantage of this representation is that it enables FRET signals that are acquired experimentally and that are proportional to the photon fluxes out of either the donor or the acceptor fluorophores to be quickly analyzed. Thus, from Equation 4, one can write:

$$E'_{FRET} = \frac{1}{1+\left(\frac{R}{R'_0}\right)^6} = \frac{I_A}{I_A + I_D}, \tag{5}$$

where I_A is the area of the acceptor emission peak and I_D is the area of the donor emission, respectively (see Materials and Methods, Eqs. 9–11).

RESULTS

Design of apta-FRET chimeras

To test if apta-FRET chimeras can rigidly orient fluorophores so as to resolve the angular dependence of FRET, structural, photophysical, and biochemical inspection of previously characterized fluorescent aptamers was performed. Of the approximately ten fluorescent aptamer classes characterized to date (Trachman and Ferré-D'Amaré 2019), the Spinach and Mango fluorescent aptamers were the most promising for apta-FRET. Both of these classes are structurally well characterized (Trachman et al. 2017b) and demonstrate reasonable spectral overlap, specificity, and affinity for their cognate fluorophores (Jeng et al. 2016). The Mango aptamers are particularly intriguing given they all induce bright fluorescence and nanomolar affinity for the fluorophores TO1-Biotin and TO3-Biotin (Supplemental Fig. S1A). Of the four Mango aptamers, only Mango-I (Trachman et al. 2017a) and Mango-III (Trachman et al. 2019a) reveal well-ordered fluorophores by X-ray crystallography. These two aptamers are structurally distinct; Mango-I links its fluorophore-binding quadruplex module with an external helix through a partially crystallographically disordered GAA^A tetraloop-like junction (^ indicates quadruplex insertion site, Fig. 1A), while the analogous helix–quadruplex junction of Mango-III is a well-defined coaxially stacked triplex (Fig. 1B). The fluorophore-binding pocket of the Spinach class aptamers resides between two coaxially stacked paired elements of variable sequence and length (Fig. 1C). This structure provides the opportunity to splice RNAs into the intervening sequence of P2 (Fig. 1D). Indeed, Spinach2 was able to incorporate an intervening $tRNA^{Lys}3$ sequence in this region (Strack et al. 2013). Lastly, the "plug and play" (Song et al. 2014) nature of both the Mango and Spinach class of aptamers makes it possible to tune spectral overlap and orthogonality.

G-quadruplex junctions vary in structural integrity

To test the feasibility of orientation-resolved FRET, chimeras of Broccoli (a variant of Spinach) and Mango-III aptamers,

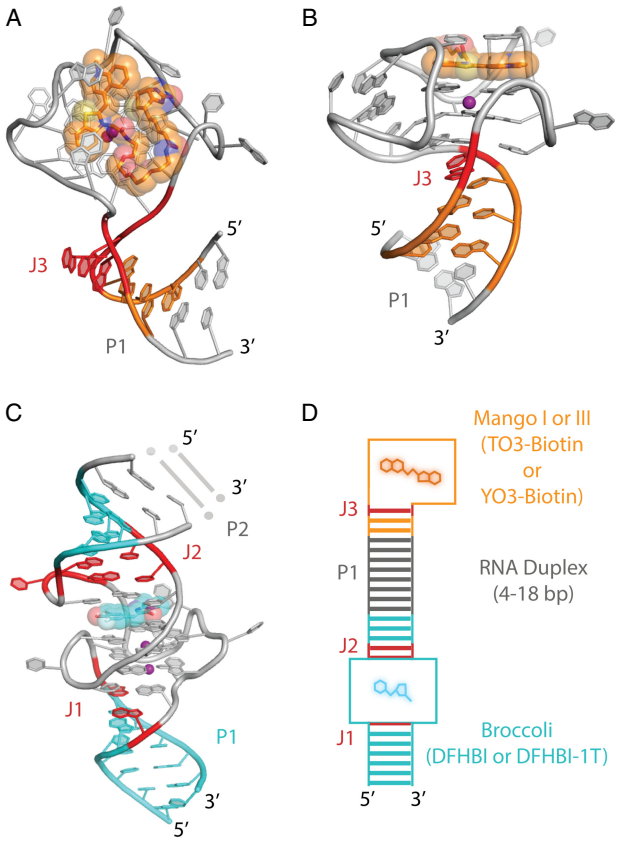

FIGURE 1. Structural comparison of fluorescent aptamers for apta-FRET. (*A*) Structure of the Mango-I aptamer (light gray, cartoon) bound to TO1-Biotin (orange stick and transparent spheres). GAA^A tetraloop-like junction (red), and helix (orange/gray) are proximally oriented to the binding pocket. (*B*) Mango-III core (light gray, cartoon) bound to TO1-Biotin (orange sticks and transparent spheres) coaxially stacked onto a helical-duplex junction (red) continuous with a variable helix (orange and gray). (*C*) Structure of Spinach (shown to represent Broccoli) bound to DFHBI (cyan sticks and transparent spheres). Coaxial helical junctions (red) are flanked by helical duplexes (cyan and gray). (*D*) Schematic representation of Broccoli (cyan)/Mango (orange) aptamers in a chimeric construct connected by an RNA duplex (gray).

separated by a canonical Watson–Crick A-form helix of variable length, were designed and transcribed. We hypothesize that the acceptor and donor dipoles found in Mango-III and Broccoli aptamers are approximately perpendicular to the spacer helix, which leads to the prediction that FRET maxima and minima should alternate every 90° of rotation about the helical axis if the fluorophores are rigid relative to the central helical axis (Eq. 2). Sequential addition of base pairs increases the distance between the two aptamers while rotating the aptamers about the helical axis. The maximum FRET signal between Broccoli-bound DFHBI (Paige et al. 2011) (donor) and Mango-III-bound TO3-Biotin (Dolgosheina et al. 2014) (acceptor) (Materials and Methods, Eq. 6; Supplemental Fig. S1A,B) was recorded while systematically changing the length of the connecting helix from 4 to 14 bp [Broc-bp-M3 constructs (Broc = Broccoli, bp = 4–14 bp, and M3 = Mango-III); Supplemental Table S1]. As the pitch of an A-form dsRNA helix is expected to be ~11 bp (Lacerda et al. 2017), a 90° rotation corresponds to ~2.75 bp of extension. These expectations correlate well with the observed pattern of maxima and minima in these data (Supplemental Fig. S1C). In contrast, a similar helical series using Mango-I and Broccoli did not exhibit such oscillations (Supplemental Fig. S1C, blue data), instead, a linearly regressing signal reminiscent of transiently helical end-stacked fluorophores was observed (Iqbal et al. 2008b). The FRET signal for the Broc-bp-M1 is consistently larger than Broc-bp-M3 for a given spacer length. While it is possible that the flexible junction of Mango-I may support reduced distances between donor and acceptor, these results are likely caused by deviation of the normal vector of the acceptor dipole and a resulting increase in κ^2. These data are consistent with the prediction that the helical junctions and fluorophore-binding cores of Mango-III and Broccoli are rigid relative to the helix, while that of Mango-I is not.

Improvement of spectral properties and specificity for an apta-FRET pair

As shown in Jepsen et al., DFHBI-1T (Song et al. 2014) and YO3-Biotin (Jepsen et al. 2018) have greater spectral overlap than DFHBI and TO3-Biotin (Jepsen et al. 2018). In order to obtain a similar spectral overlap, we used DFHBI-1T in the Broccoli pocket and YO3-Biotin as the acceptor in the Mango-III pocket (Supplemental Fig. S2A) and found that these fluorophores show greater orthogonality since DFHBI-1T and YO3-Biotin bind with greater specificity to Broccoli and Mango-III, respectively (Table 1). Specificity is required for interpretable FRET results when using apta-FRET. There are nine potential occupancy states for a biomolecule with two independent binding sites and two distinct ligands. Of these combinations, only four binding-states modify the FRET signal; single occupancy of DFHBI-1T in either (i) Mango-III or (ii) Broccoli binding pocket, (iii) double occupancy of Mango-III and Broccoli by DFHBI-1T, and (iv) Mango-III bound to DFHBI-1T and Broccoli bound to YO3-Biotin. The first three states (i–iii) would give rise to underestimated E'_{FRET} values since no acceptor is present (Eq. 5). Only binding state (iv) would confound orientational FRET. Fortunately, Mango-III binds with high specificity and affinity to YO3-Biotin, while Broccoli binds YO3-Biotin weakly (Table 1, and Materials and Methods). DFHBI-1T can be displaced from the Broccoli binding pocket, but only at high concentration of YO3-Biotin (Jepsen et al. 2018). Finally, in apta-FRET experiments, one could reasonably expect fluorescent signals to result from low levels of nonspecific fluorophore-bound states other than from fluorophore-aptamer binding. This matter will be addressed in the sections "Generation of structural models for FRET simulation" and "FRET lifetimes." However, titration of YO3-Biotin results in increased FRET with a reduction of DFHBI-1T fluorescence emission due to energy transfer (Supplemental Fig. S2C).

FRET oscillates as a function of connecting duplex length using Broc-bp-M3 constructs

FRET was measured for the Broc-bp-M3 (M3 = Mango-III) series of constructs extending from 4 to 18 bp (~1.4 turns of an A-form RNA duplex) using DFHBI-1T and YO3-Biotin fluorophores. Triple gaussians were fit to the donor and acceptor emission peaks to accurately determine their relative areas (Fig. 2A; Supplemental Table S2). The

TABLE 1. Binding affinity and excitation/emission peaks of Broccoli and Mango-III with DFHBI, DFHBI-1T, TO3-Biotin, and YO3-Biotin

	Broccoli		Mango-III	
	EC_{50} (nM)	ex/em max (nm)	EC_{50} (nM)	ex/em max (nm)
DFHBI	420 ± 40[a]	469/503[a]	>>	n/a
TO3-Biotin	22 ± 10	637/658	25 ± 2	625/655
DFHBI-1T	270 ± 10	473/505	>>	n/a
YO3-Biotin	910 ± 40	592/615	10 ± 0.2	595/620

(>>) EC_{50} was greater than detection limit of assay.
[a]Values were measured with the Spinach aptamer and obtained from a previous study (Jeng et al. 2016).

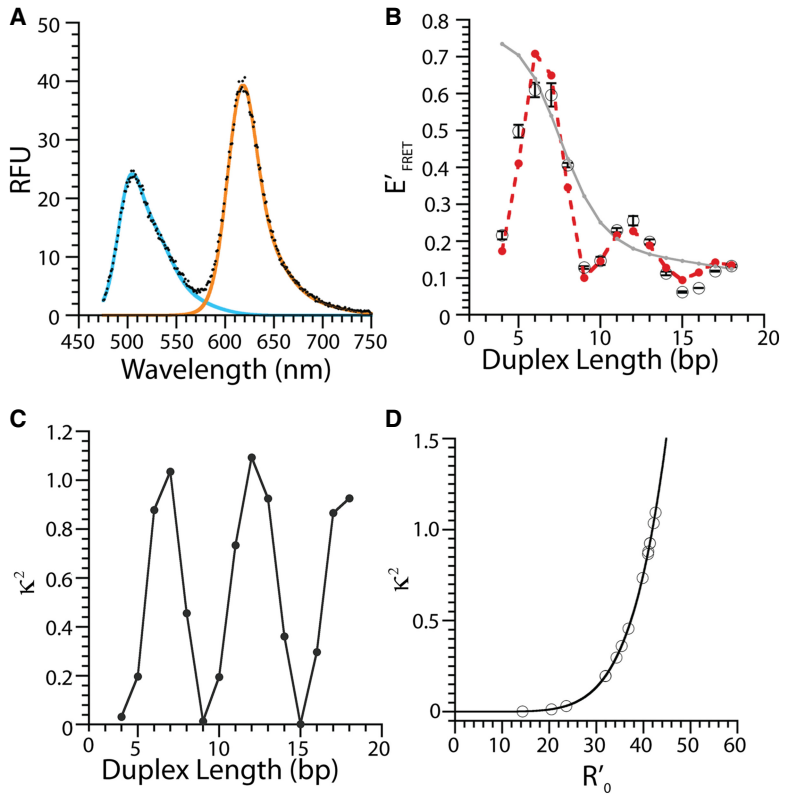

FIGURE 2. FRET efficiency as a function of duplex length. (*A*) FRET signal observed for the Broc-6bp-M3 duplex fit to a three parameter gaussian for the DFHBI-1T donor (blue) and YO3-Biotin acceptor (orange) (see Supplemental Fig. S3 for full set). (*B*) FRET efficiency as a function of helical extension calculated using Equations 4 and 5. Open black circles represent the averaged data points. Red circles with dashed red line represent the values fitted using the structural models. Gray line indicates the poor correlation of simulated data using a constant κ^2 value of 2/3. (*C*) κ^2 values determined from the model analysis over the apta-FRET series. (*D*) R'_0 calculated for the observe apta-FRET κ^2 range.

residuals from these fits are small (Supplemental Fig. S3; Supplemental Table S2), allowing extraction of donor and acceptor emission peak areas. Using the fitted peak areas, E'_{FRET} was calculated by taking the ratio of the acceptor peak area to the sum of the donor and acceptor areas (Eqs. 5, 10, and 11). As seen with our initial trial with DFHBI and TO3-Biotin, oscillations in E'_{FRET} tracked precisely with the 11 bp per helical turn of an A-form duplex. Three local maxima and two local minima are observed with maxima being displaced by 5–6 bp (Fig. 2B; Supplemental Table S3). Therefore, the fluorophore-binding cores of Broccoli and Mango-III rigidly orient the improved FRET pairs DFHBI-1T and YO3-Biotin.

Mango-III–YO3-Biotin and iSpinach–DFHBI-1T cocrystal structures

To help determine the relative orientation of the excitation and emission fluorophore dipoles in each of the complexes shown in Figure 1D, and to facilitate accurate model building, the cocrystal structures of Mango-III–YO3-Biotin and *i*Spinach–DFHBI-1T were determined. The cocrystal structure of YO3-Biotin in complex with Mango-III was solved at 2.8 Å resolution (Supplemental Table S4) by molecular replacement (the structure of the Mango-III–TO1-Biotin complex (Trachman et al. 2019a), without the fluorophore, was used as the search model). The Mango-III–YO3-Biotin complex superimposed closely on that of the Mango-III–TO1-Biotin complex, with a root mean squared deviation (RMSD) of 0.24 Å for all non-hydrogen atoms. Residual electron density corresponding to the (*E*) conformation of YO3-Biotin was observed and modeled into the binding pocket (Fig. 3A). Structural superposition of the Mango-III–YO3-Biotin binding pocket onto the Mango-III–TO1-Biotin binding pocket yields an RMSD value of 0.23 Å (Fig. 3B). The fluorophores are highly similar in binding pocket location and overall orientation.

To determine if structural and orientation differences exist between DFHBI and DFHBI-1T, we determined the cocrystal structure of *i*Spinach–DFHBI-1T. The *i*Spinach aptamer (Autour et al. 2016; Fernandez-Millan et al. 2017) was chosen for structural characterization in complex with DFHBI-1T for three reasons: (i) a high resolution structure of the Broccoli aptamer has not yet been reported, (ii) sequence alignment of all three DFHBI-1T aptamers and structural superposition of *i*Spinach–DFHBI and Spinach–DFHBI (RMSD 0.24 Å) suggest highly similar binding pocket structures (Supplemental Fig. S4), and (iii) of the Spinach-derived aptamers (Spinach, *i*Spinach, and Broccoli), the *i*Spinach crystallizing construct achieves the highest resolution, and therefore greatest model precision (Fernandez-Millan et al. 2017). The *i*Spinach–DFHBI-1T cocrystal structure was determined at 2.1 Å resolution by molecular replacement (using the *i*Spinach–DFHBI structure with the fluorophore omitted as the search model). Residual electron density was observed for the DFHBI-1T fluorophore in the binding pocket (Fig. 3C,D). The trifluoroethane substitution, which distinguishes DFHBI from DFHBI-1T, is packed in a groove formed by residues A22, A45, and A50 (Fig. 3D) and likely prevents sliding of the fluorophore in the binding pocket. The *i*Spinach–DFHBI-1T binding pocket is highly similar to the *i*Spinach–DFHBI and Spinach–DFHBI-1T binding pockets

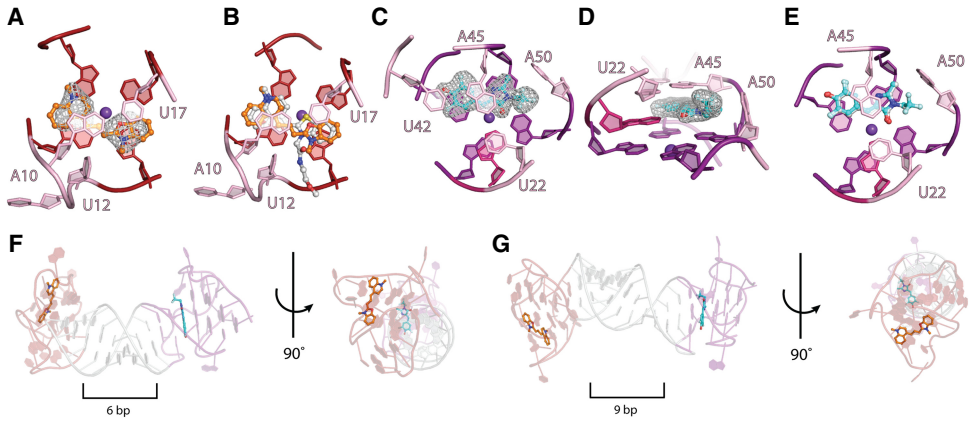

FIGURE 3. Structural characterization of the apta-FRET complexes and chimeras. (*A*) Binding pocket of Mango-III (cartoon) bound to YO3-Biotin (orange, ball-stick). $|F_o| - |F_c|$ electron density map prior to ligand placement contoured at 2.0 σ is shown in gray mesh. (*B*) Structural superposition of Mango-III/YO3-Biotin and Mango-III/TO1-Biotin (PDB: 6E8S) binding pockets. Binding pocket of the Mango-III/YO3-Biotin complex (cartoon) with YO3-Biotin (orange, ball-stick) and TO1-Biotin (gray, ball-stick). (*C*) Binding pocket of *i*Spinach (cartoon) bound to DFHBI-1T (cyan, ball-stick). $|F_o| - |F_c|$ electron density map prior to ligand placement contoured at 2.5 σ (gray mesh). (*D*) 90° rotation of (*C*) highlighting trifluoromethane packing against residue A50. (*E*) Structural superposition of non-hydrogen, RNA atoms of *i*Spinach/DFHBI-1T and *i*Spinach/DFHBI (PDB: 5OB3) binding pockets. *i*Spinach/DFHBI-1T complex (cartoon) with DFHBI-1T (cyan, ball-stick) and DFHBI (gray, ball-stick). (*F*) Structural model of Broc-6bp-M3 with *side* (*left*) and *top* (*right*) views demonstrating parallel dipole alignment. (*G*) Structural model of Broc-9bp-M3 with *side* (*left*) and *top* (*right*) views demonstrating perpendicular dipole alignment. P1 helices (see Fig. 1D) in panels *F* and *G* are deleted for clarity.

with RMSD values of 0.17 and 0.41 Å, respectively (Fig. 3E; Supplemental Fig. S4). Thus, the structure of *i*Spinach–DFHBI-1T complex likely captures the molecular details necessary to accurately model the Broccoli–DFHBI-1T aptamer.

Generation of structural models for FRET simulation

Using the *i*Spinach–DFHBI-1T and Mango-III–YO3-Biotin crystal structures, a set of 3D models for the helical apta-FRET chimeras were constructed to enable FRET simulation (Fig. 3F,G; Supplemental Structure Files). Radii of gyration (R_gs), calculated from these structural models, were in fair agreement with the R_gs measured by SAXS (Supplemental Fig. S5). In addition, molecular envelopes calculated from the SAXS data overlaid well with the models, revealing a consistent kink in the helical axis below the two fluorophore-binding pockets (Supplemental Fig. S5). from SAXS and were therefore used to report the static fluorophore positions for the entire Broc-bp-M3 series (Supplemental Table S1). The YO3-Biotin and DFHBI-1T fluorophores bind to their respective aptamers in a near planar conformation. Assuming the fluorophore dipoles are within the plane of the conjugated-bond network (Lacerda et al. 2017), a coordinate system uniquely parameterizing the acceptor and donor dipole orientations was created using a clock-face type notation (Supplemental Fig. S6).

FRET data for the entire set of models were fit by rotating the acceptor and donor vectors around this clock face, while fitting by least squares the E'_{FRET} data (Supplemental Table S5) to the theoretical expectation summarized in Equation 5. A fit to the data was obtained (Fig. 2B; Materials and Methods) with fitted κ^2 values ranging between 0 to ~1.1 and R'_0 values ranging from 14 to 42 Å (Fig. 2C,D). While in principle a three-parameter fit corresponding to the two clock-face angles ($0 < \theta_{DFHBI\text{-}1T} < 360°$; $0 < \gamma_{YO3\text{-}Biotin} < 360°$) and the coefficient $\beta = \alpha\phi_A$ should be sufficient, a linear factor $m = 0.096$ (±0.046) was required to satisfactorily fit the experimental data (Eqs. 11 and 12). We attribute this small term to nonspecific binding which results in rotationally averaged fluorescence. We found $\alpha\phi_A = \beta = 5.43$ (± 2.21) × 10^9, $\theta_{DFHBI\text{-}1T} = +44$ (±95) degrees, $\gamma_{YO3\text{-}Biotin} = 45$ (± 95) degrees. Consistent with the clock face of both the donor and acceptor fluorophore being ~90° to the A-form helical axis, fixing the absolute orientation of the acceptor dipoles was challenging. Nevertheless the residual of the χ^2 fit (Eq. 13) plotted as a function of θ and γ indicate the high correlation between our initial choice in donor and acceptor orientation 12 o'clock orientation (i.e., $\theta = 0$ and $\gamma = 0$ as shown in Supplemental Fig. S6) and the overall quality of the fit (Supplemental Fig. S7A,B). If the fluorophores are not constrained and κ^2 is taken as an average of 2/3, then R'_0 for this FRET series was found to be ~40 Å (Fig. 2B). Taken together, these data support the initial hypotheses that the fluorophore dipole vectors are perpendicular to the helical axis and the variable helix is rigid over the length scale tested.

FRET lifetimes

The measurement of FRET in the time domain has several advantages over steady-state data. Time-resolved FRET can measure heterogeneity in a FRET population, interference from the direct excitation of the acceptor, and

polarized transients due to observed segmental mobility, nonspecifically bound fluorophore, and discrete angles between fluorophores. To measure FRET lifetime, we measured the donor decay in the presence of acceptor $I_{D'}$ and the acceptor decay I_A, so that τ' appears with a negative preexponential (Eq. 6b):

$$I_{D'}(t) = \alpha e^{-t/\tau'}, \tag{6a}$$

$$I_A(t) = -\beta e^{-t/\tau'} + \beta e^{-t/\tau A}, \tag{6b}$$

where τ_A is the lifetime of the acceptor. From these data we assessed that direct excitation of the acceptor, YO3-Biotin, was minimal. In the presence of direct excitation of acceptor by donor laser, the two β terms do not match and $I_A(t)$ begins above zero. By providing an ~3 µM excess of RNA over the fluorophore, free dye is virtually nonexistent owing to the high affinity of these aptamers for their cognate fluorophores. Lifetimes of the individual fluorophores in the absence of FRET counterparts were fit best with a single exponential decay while lifetime traces of the FRET pair complex were best fit with two lifetimes (Supplemental Table S6; Supplemental Fig. S8). An additional short lifetime was included as needed (~0.05 nsec) which accounted for <1% of fluorescence lifetime intensity and is likely a result of nonspecific fluorophore binding. The main contributing lifetime of the donor/acceptor pairs is strongly influenced by changes in κ^2 and the distance between the fluorophore pair. Fluorophores parallel or closer to each other (large κ^2 or fewer base pair spacers, respectively) have shorter lifetimes than constructs with perpendicular fluorophores or that are further apart. The efficiency of the energy transfer (E_τ) between the donor and acceptor, with τ_D corresponding to the lifetime with only the donor present and τ_{DA} corresponding to the lifetime with both donor and acceptor present, is given by Equation 7:

$$E_\tau = 1 - \left(\frac{\tau_{DA}}{\tau_D}\right). \tag{7}$$

Using Equation 7, the efficiency of the energy transfer decreased with increasing bp with 6, 8, and 9 bp having FRET efficiencies of 0.83 (+0.3, −0.1), 0.68 (+0.07, −0.1), and 0.19 (+0.5, −0.3), respectively. These values agree with the corresponding loss of steady-state FRET efficiency (E_{FRET}') observed in Figure 2B as the fluorophore pair rotate from approximately parallel to perpendicular.

The chromophores in both the donor and acceptor sites predominantly report a rigid conformation with overall tumbling in the 15–20 nsec range, as expected based on mass. The internal angles between excitation and emission dipoles in each chromophore are significant, reducing the measurable anisotropy even in the absence of FRET, thus making precise recovery of transfer angles from transferred anisotropy difficult. This system would thus need to be excited at multiple wavelengths, collected to very high signal to noise ratios, and subjected to a global analysis to attempt recovery of transferred anisotropy angles.

Orientation dependence of FRET in the NiCo riboswitch

The NiCo riboswitch is composed of a four-way helical junction that forms a cruciform shape upon binding Ni^{2+} or Co^{2+} and folds without any long-range tertiary interactions. To study the flexibility of the complex RNA junction at the core of the NiCo riboswitch (Furukawa et al. 2015) apta-FRET pairs were incorporated into the helical paired elements, P2 and P4 (Fig. 4A). Insertion of Mango-III into P2 and Broccoli into P4 provided an E'_{FRET} response upon titration of Co^{2+} (Fig. 4B) which fit to a binding isotherm with a Hill coefficient of 1.9 and an $EC_{50} = 0.84 \pm 0.05$ µM. These data are consistent with previous results from in-line probing analysis (Furukawa et al. 2015) and a chimeric Spinach2 sensor assay (Xu and Cotruvo 2020). The E'_{FRET} value measured in the absence of Co^{2+} was

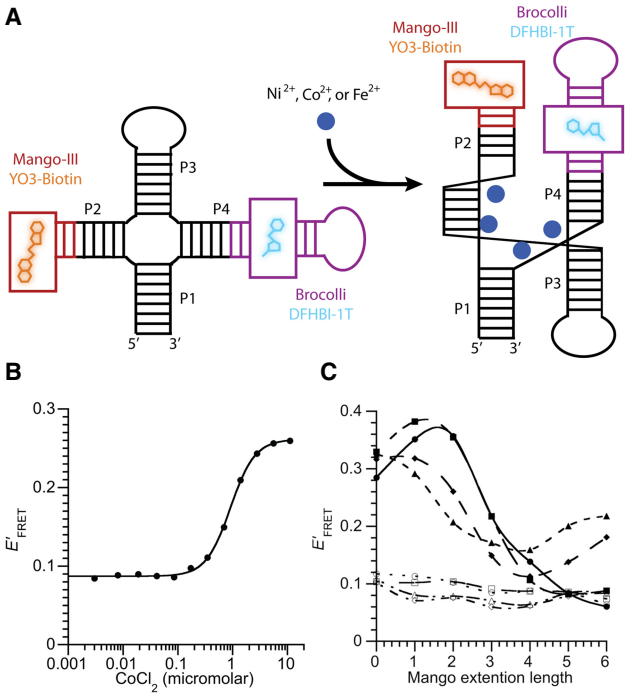

FIGURE 4. NiCo riboswitch apta-FRET. (*A*) Secondary structure of the NiCo riboswitch and aptamer insertions (*left*). Relative organization of NiCo apta-FRET chimera sites upon folding (*right*). (*B*) E'_{FRET} signal resulting from a Co^{2+} titration of construct 27 (see Supplemental Table S1), fit to the Hill equation. (*C*) E'_{FRET} observed for each of the NiCo apta-FRET chimeras plotted as a function of the Mango-III, P2 helical extension. The corresponding Broccoli P4 extension is indicated by circles: 0 bp; squares: 1 bp; diamonds: 2 bp; and triangles: 3 bp (see Supplemental Table S1 for the full set of sequences). Closed symbols indicate the presence of 10 µM $CoCl_2$, open symbols are in the absence of $CoCl_2$. As a visual aid, data points are connected by smooth curves.

0.09, likely resulting from intrinsic flexibility of the four-way junction in the absence of Co^{2+}.

To test if orientation-dependent FRET could be resolved in the NiCo riboswitch, a series of seven Mango-III helical extensions in P2 were combined with a series of four Broccoli helical extensions in P4, for a total of 28 RNA constructs (Supplemental Table S1). E'_{FRET} was measured for each construct in the presence or absence of 10 μM $CoCl_2$ (Fig. 4C). In the absence of Co^{2+}, E'_{FRET} values were small, averaging 0.09 ± 0.025, and only weakly dependent on the site of insertion of the Mango-III or Broccoli aptamer (Fig. 4C). The average E'_{FRET} value is consistent with an extended form of the riboswitch and supports a flexible four-way helical junction. In the presence of Co^{2+} ions, E'_{FRET} values significantly increased and showed a sinusoidal pattern with extension of the Mango-III aptamer along the P2 helix. The phase and intensity of these signals change as a function of the Broccoli extension along the P4 helix (Fig. 4C), consistent with rigid rotation about either helical axis. The seven Mango-III constructs tested correspond to a rotation of some 230° about the P2 stem and a corresponding movement away from the core of the riboswitch (Fig. 4A) of ~25 Å, whereas the four Broccoli variants correspond to a rotation of some 130° and extension of 14 Å along the P4 stem. Based on the available X-ray structure of the NiCo riboswitch the P2 and P4 helices are inclined with respect to each other by about 80° (Furukawa et al. 2015). The noncoplanar locations of Mango-III and Broccoli will pass each other in a nontrivial geometry consistent with the changes in phase observed in our data set.

DISCUSSION

The utility and ability to visualize RNA using fluorescent aptamers in live cells is well established (Strack et al. 2013; Autour et al. 2018; Jepsen et al. 2018; Cawte et al. 2020). To further advance RNA imaging techniques, we have now systematically characterized and assessed fluorescent aptamers for performing orientation-dependent FRET. The apta-FRET pairs used here have R'_0 values ranging from nearly zero to up to ~50 Å. This falls within the range of optimal Förster radii (10–100 Å) traditionally needed to study biological macromolecules. This is comparable to the R_0 of most fluorescent protein (Bajar et al. 2016) and small molecule FRET pairs (Wu and Brand 1994). In addition, the fluorescent lifetimes of these systems were observed to range from 4.7 to 1.2 nsec and are therefore well-suited for existing fluorescence lifetime imaging (FLIM) microscopy techniques (Lakowicz et al. 1992a,b). Further development and characterization of fluorescent aptamers will likely expand the available techniques for imaging RNA in live cells.

Previous FRET studies of RNA duplex and three-way junctions utilized transiently end-stacked cyanine dye FRET pairs under the assumption that fluorophores were oriented completely in parallel (Iqbal et al. 2008a; Fessl and Lilley 2013). The transient end-stacking of cyanine dyes dampened the angle-dependent effect on FRET. The rigid binding of fluorophores using the fluorogenic aptamers Broccoli and Mango-III does not have this effect, revealing steep peaks and troughs as a function of helix length and twist. By substituting the FRET acceptor Mango-III for Mango-I, we observed that FRET linearly regressed in a manner similar to radially averaged cyanine dye derivatives. These data demonstrate that not all fluorogenic aptamers are rigidly connected to their helical stems and that the rigidity of helical junctions can be assessed through orientation-resolved FRET. Indeed, the Co^{2+}-bound NiCo riboswitch demonstrated similar sinusoidal FRET response to Broc-bp-M3 upon helical extension despite having a complex four-way junction. These data are surprising given NiCo lacks long-range tertiary contacts to facilitate positioning of apta-FRET pairs, demonstrating the robust nature of the apta-FRET system.

A significant advantage of angular-resolved FRET is that a small angular rotation, with static fluorophore distance, can result in a large change in FRET signal (Eq. 2). Single-molecule FRET studies using rotationally averaged fluorophores have concluded that multistep folding pathways are required for both cognate and reactive folding pathways of riboswitches and ribozymes, respectively (Tan et al. 2003; Nahas et al. 2004; Suddala et al. 2019). Thus angle-dependent apta-FRET can be expected to inform on a variety of previously undetectable conformational changes with consequent improvements in structural interpretation. It should be noted that when implementing rigid fluorophores to measure distances using FRET, one must take caution to accurately determine κ^2 rather than assume a disordered FRET pair. Large oscillations in κ^2 may give rise to incorrect relative distances.

While the current study focused on organization of RNA junctions void of protein cofactors, research on ribonucleoprotein interactions will likely benefit from the sensitivity of apta-FRET reporters. The ubiquitous 50° angle of the kink-turn motif can be induced by protein binding partners; however, many of these RNAs are prefolded by Mg^{2+} alone (Huang and Lilley 2016). Angular-dependent FRET will likely be required to resolve the subtle changes induced by protein binding in these and other systems such as the spliceosome, ribosome and numerous lncRNAs, already, and yet to be discovered.

MATERIALS AND METHODS

Broc-bp-M3 and Broc-bp-M1 FRET measurements

All fluorescence data are steady state measurements using a Varian Cary Eclipse fluorescence spectrophotometer at room temperature. Experiments were performed in 140 mM KCl,

10 mM NaH_2PO_4 pH 7.2, 1 mM $MgCl_2$, 0.05% Tween-20. Samples containing 30 nM RNA, 1.5 µM DFHBI-1T and 200 nM YO3-Biotin were incubated at RT for 1 h then exciting at 460 nm and emission scanned at a rate of 1 nm/sec from 475–750 nm at 25°C. The potential difference in the photomultiplier tube was set to 800 V and ex/em slit widths at 5/10 mm, respectively.

RNA for these experiments was transcribed from dsDNA templates using T7 RNAP as described elsewhere (Trachman et al. 2020).

For the Broc-nbp-M1 series, concentrations are as follows: 500 nM RNA, 3 µM DFHBI, 3 µM TO3-Biotin. For the Broc-nbp-M3 series, 500 nM RNA, 3 µM DFHBI, 200 nM TO3-Biotin. Here, we estimated apta-FRET transfer efficiency (E'_{FRET}) by taking the maximum peak heights of the TO3 emission and dividing it by the sum of the DFHBI and TO3 emission peak heights as follows:

$$FRET_S = \frac{S_{TO3}}{S_{TO3} + S_{DFHBI}}. \quad (8)$$

FRET spectrum fitting for DFHBI and YO3 fluorophores

Raw FRET spectra were fit to preassigned Gaussians using the following equation:

$$F = n1\left(e^{-\left(\frac{\lambda-500.5+m1}{16.35}\right)^2} + 0.8409e^{-\left(\frac{\lambda-520.2+m1}{28.47}\right)^2} + 0.2574e^{-\left(\frac{\lambda-544+m1}{47.58}\right)^2}\right) + n2\left(e^{-\left(\frac{\lambda-616.1+m2}{20.42}\right)^2} + 0.3175e^{-\left(\frac{\lambda-634.3+m2}{34.3}\right)^2} + 0.0904e^{-\left(\frac{\lambda-663.5+m2}{58.73}\right)^2}\right) \quad (9)$$

The fluorescence signal F resulting from donor and acceptor emission was fit as follows: n1 and m1 are the Y-scaling factors and a small term to correct for wavelength shift, respectively of the donor Broccoli–DFHBI-1T Gaussians. Correspondingly, n2 and m2 serve the same function for the Mango–YO3-Biotin acceptor Gaussians. Gaussian peak shapes were predetermined by fitting the emission of Broccoli/DFHBI-1T without acceptor fluorophore and the Mango–YO3-Biotin emission spectrum in the absence of donor fluorophore. Emission peak shifts between each construct as defined by m1 and m2 were found to be small and relatively insignificant (Supplemental Table S2).

E'_{FRET} values were calculated by integration of the two Gaussian groups after fitting n1, n2, m1, and m2 parameters in Equation 6. The Broccoli–DFHBI-1T emission peak area being:

$$I_D = \int_0^\infty n1\left(e^{-\left(\frac{\lambda-500.5+m1}{16.35}\right)^2} + 0.8409e^{-\left(\frac{\lambda-520.2+m1}{28.47}\right)^2} + 0.2574e^{-\left(\frac{\lambda-544+m1}{47.58}\right)^2}\right)d\lambda. \quad (10)$$

The Mango–YO3-Biotin emission integral being:

$$I_A = \int_0^\infty n2\left(e^{-\left(\frac{\lambda-616.1+m2}{20.42}\right)^2} + 0.3175e^{-\left(\frac{\lambda-634.3+m2}{34.3}\right)^2} + 0.0904e^{-\left(\frac{\lambda-663.5+m2}{58.73}\right)^2}\right)d\lambda. \quad (11)$$

Small angle X-ray scattering

RNA was transcribed from synthetic DNA as described previously (Trachman et al. 2018) and treated prior to shipment as described previously (Lau et al. 2017). Briefly, transcripts were purified on a 12% (19:1) polyacrylamide gel, 8 M Urea, 1x TBE. RNA was electo-eluted from gel slices and exchanged into Buffer A (20 mM MOPS pH 7.5, 150 mM KCl, 1 mM $MgCl_2$, 1 µM DFHBI, 0.1 µM YO3-Biotin) after addition of an equal molar ratio of DFHBI and YO3-Biotin to occupy all binding sites on the RNA. Transcripts were annealed by heating to 95°C for 3 min followed cooling on ice. Transcripts underwent size exclusion purification on an AKTApurifier with a Superdex200 Increase column (GE Healthcare) equilibrated with Buffer A. Monomeric species were collected and subjected for small angle X-ray scattering measurements (SAXS).

SAXS was performed at the Advanced Photon Source, beamline 12-ID-B (APS 12-ID-B). Data were collected on a Pilatus 2M detector at a beam energy of 14 keV. Forty measurements were taken per sample with a 0.5 sec exposure time and a 2 sec delay between measurements. Samples were passed through a flow cell to reduce radiation damage during collection. Radially averaged data for all 40 measurements were plotted and checked for outliers due to air contamination. Scattering curve averaging and buffer subtraction was performed in IgorPro.

Data were analyzed using the ATSAS program suite. The radius of gyration (R_g) and maximum scattering distance (D_{Max}) was calculated using AUTORG (Petoukhov and Svergun 2007). These parameters were provided to GNOM (Svergun 1992), without specifying shape constraints, to generate P(*r*) plots. The output from GNOM was input into DAMMIF (Franke and Svergun 2009), without prior assumption of shape, using a random seed, 20 harmonics, 4 Å dummy atom radius, and nine Shannon channels for 200 steps. Ten DAMMIF simulations were performed in succession. Dummy atom coordinates from all 10 DAMMIF simulations were provided to Damaver (Volkov and Svergun 2003) pipeline and filtered with Damfilt (Volkov and Svergun 2003). The refined SAXS envelopes were then fit to the modeled chimeras using SUPCOMB (Kozin and Svergun 2001). The R_gs for the modeled chimeras were determined using CRYSOL (Svergun et al. 1995).

X-ray crystallography

RNA was in vitro transcribed and exchanged into buffer as described previously (Trachman and Draper 2017). *i*Spinach was exchanged into 40 mM Tris-HCl pH 7.5, 100 mM KCl, 1 mM $MgCl_2$ with the addition of DFHBI-1T in a molar ratio of 1:1.2 after exchange. The solution was heated to 85°C and cooled to 25°C (−1.5°C/min). *i*Spinach–DFHBI-1T cocrystals were grown by vapor diffusion at 21°C. Sitting drops were prepared by mixing 0.2 µL of the RNA-fluorophore mixture (210 µM RNA and 252 µM fluorophore) with the same volume of a reservoir solution comprised of 40 mM Na cacodylate pH 7.0, 40 mM NaCl, 12 mM spermine hydrochloride, 32% (v/v) 2-methyl-2,4-pentanediol (MPD). Crystals were cryo-protected in a solution of 40 mM Na cacodylate pH 7.0, 40 mM Tris-HCl pH 7.5, 12 mM spermine, 100 mM KCl, 1 mM $MgCl_2$, 46% (v/v) MPD, and 10% (v/v) glycerol. Mango-III was exchanged into 20 mM MOPS pH 7.0, 150 mM KCl, and 10 µM EDTA. The RNA was annealed by heating 95°C for 1 min and then cooled on bench, at room temperature, for 10 min. For crystallization, an equimolar ratio of YO3-Biotin was added and 0.2 µL of RNA solution was added to 0.2 µL to reservoir solution (40 mM Na cacadylate pH 7.0, 80 mM NaCl, 12 mM KCl, 1 mM $MgCl_2$, 10 mM Spermine, 5% sucrose, and 33% 2-methyl-2,4-

pentanediol). Additional cryo-protection was not necessary for preparing crystals. Both *i*Spinach and Mango-III crystals were mounted in nylon loops and flash frozen by plunging into liquid nitrogen.

Diffraction data were collected at 100 K using the rotation method at beamline 24-ID-C of the Advanced Photon Source (APS) and integrated and scaled using XDS (Kabsch 2010). Phase solutions were obtained by the program Phaser (McCoy et al. 2007) using the PDB deposits 5OB3 and 6E8S, with the ligands and ions removed from the search model, for *i*Spinach and Mango-III, respectively. Refinements were carried out in phenix.refine (Afonine et al. 2012) with iterative rounds of building and simulated annealing, energy minimization, and *B*-factor refinement. Data are summarized in Supplemental Table S4.

Structure models and corresponding model parameters

Structural models of Broc-nbp-M3 constructs were generated from the crystal structures of Mango-III–YO3-B described here, *i*Spinach–DFHBI-1T and an A-form RNA duplex (Tolbert et al. 2010). Models were built using a combination of UCSF Chimera (Lacerda et al. 2017), PyMol (The PyMOL Molecular Graphics System, Version 1.2r3pre, Schrödinger, LLC). and python scripts (Supplemental Material). The main parameters extracted from these models were: R_i the distance vector from the donor to the acceptor and the unit vectors: a_1 and d_1 that are perpendicular to the "clock-face" that defines the area contained by either the acceptor or donor fluorophore respectively and are determined by principal component analysis using MatLab software.

Model fitting to FRET data

A MatLab script was built to model the helical data set. For the ith E'_{FRET} model, values were calculated as follows:

$$E'_{FIT,i} = \frac{\beta k(\theta, \gamma)_i^2}{\beta k(\theta, \gamma)_i^2 + R^6} + m. \quad (12)$$

Here, the donor and acceptor dipoles are allowed to explore each clock-face angle (i.e., from $0 < \theta < 360°$ in the clock-face coordinate system for the DFHBI-1T dipole and $0 < \gamma < 360$ for YO3-B), and since structural models were built for each helical construct, this allowed the calculation of $\kappa(\theta,\gamma)_i^2$ as a function of these two angles for the i^{th} model. The parameter $\beta = \alpha\phi_A$ was in principle directly calculable but was fit as free parameter of the model. The parameter *m* is not theoretically justified but was required to satisfactorily fit an offset found in the data that likely resulted from a small amount of rotationally averaged signal common to all samples. The parameters θ, γ, β, and m were then fit by minimizing:

$$\chi(\theta, \gamma, \beta, m)^2 = \sum_{i=1}^{N} (E'_{Data,i} - E'_{Fit,i}(\theta, \gamma, \beta, m))^2. \quad (13)$$

NiCo riboswitch series

RNAs where produced by transcription and E'_{FRET} measured as described for the Broc-nbp-M3 constructs except for the addition of the indicated amounts of $CoCl_2$.

Fluorescence lifetime measurements

For 412 nm excitation, a Coherent Mira 900-D Ti:sapphire laser (76 MHz, fs configuration) was tuned to 825 nm before being pulse picked with a ConOptics Electro-Optic Modulator (Model 350-160-02) and frequency doubled with a BBO crystal. For 570 nm excitation, a Spectra Physics Vanguard 2000-HM532 NdYVO4 synchronously pumped a tunable Spectra Physics Model 3500 (4 MHz) cavity dumped dye laser containing rhodamine 6G. Emissions were collected and detected with a JYH10 monochromator (8 nm bandwidth) and a Peltier cooled Hamamatsu MCP photomultiplier.

All samples were excited vertically; emissions were collected at 55° for lifetime measurements and at 0° and 90° for anisotropy measurements. Lifetimes were obtained by fitting the decay data to a multiexponential model using χ^2, the residuals, and their autocorrelation as a measure of quality. The instrument response function (typically < 150 psec) was recorded at the excitation wavelengths from a light scattering suspension of dilute colloidal silica.

DATA DEPOSITION

Analyzed data and primary data are available upon request to the corresponding authors. Coordinates and structure factors have been deposited to the Protein Database under accession codes PDB: 6UP0 and 7L0Z.

SUPPLEMENTAL MATERIAL

Supplemental material is available for this article.

ACKNOWLEDGMENTS

We thank members of the Andersen, Ferré-D'Amaré, Knutson, and Unrau laboratories for discussions. We thank A. Buller (University of Wisconsin, Madison), K. Suddala (The National Institute of Diabetes and Digestive and Kidney Diseases [NIDDK], National Institutes of Health [NIH]), and G. Piszczek of the Biophysics Core of the National Heart, Lung, and Blood Institute (NHLBI) for helpful discussions and Y-X. Wang and L. Fan of the National Cancer Institute and X. Zuo of APS sector 12 for SAXS support. We also thank the staff of beamlines 5.0.1 and 5.0.2 of the Advanced Light Source, Lawrence Berkeley National Laboratory (ALS), and 24-ID-C of the Advanced Photon Source, Argonne National Laboratory (APS) for crystallographic data collection. This research used resources of the Advanced Photon Source, a U.S. Department of Energy (DOE) Office of Science User Facility operated for the DOE Office of Science by Argonne National Laboratory under contract no. DE-AC02-06CH11357. This work is based upon research conducted at the Northeastern Collaborative Access Team beamlines, which are funded by the National Institute of General Medical Sciences from the National Institutes of Health (P30 GM124165). The Pilatus 6M detector on 24-ID-C beamline is funded by a NIH-ORIP HEI grant (S10 RR029205). This work was partially supported by a Natural Sciences and Engineering Research Council (NSERC, Canada) operating grant (P.J.U.), the European Research Council (ERC) (grant no. 683305) and the

Independent Research Fund Denmark (4181-00573A) to E.S.A., and the Intramural Program of the NHLBI, NIH.

Author contributions: S.J., R.J.T., F.W., L.T., and K.A.L. performed research. S.J., R.J.T., F.W., L.T., K.A.L., P.J.U., and J.R.K. analyzed data. A.R.F., P.J.U., J.R.K., M.D.E.J., and E.S.A. contributed reagents and analytical tools. R.J.T., S.J., and P.J.U. wrote the manuscript with contributions from all authors.

Received October 28, 2020; accepted December 20, 2020.

REFERENCES

Afonine P, Grosse-Kunstleve R, Echols N, Headd J, Moriarty N, Mustyakimov M, Terwilliger T, Urzhumtsev A, Zwart P, Adams P. 2012. Towards automated crystallographic structure refinement with phenix.refine. *Acta Crystallogr D Biol Crystallogr* **68:** 352–367. doi:10.1107/S0907444912001308

Autour A, Westhof E, Ryckelynck M. 2016. iSpinach: a fluorogenic RNA aptamer optimized for in vitro applications. *Nucleic Acids Res* **44:** 2491–2500. doi:10.1093/nar/gkw083

Autour A, Jeng S CY, Cawte A D, Abdolahzadeh A, Galli A, Panchapakesan SSS, Rueda D, Ryckelynck M, Unrau PJ. 2018. Fluorogenic RNA Mango aptamers for imaging small non-coding RNAs in mammalian cells. *Nat Commun* **9:** 656. doi:10.1038/s41467-018-02993-8

Bajar BT, Wang ES, Zhang S, Lin MZ, Chu J. 2016. A guide to fluorescent protein FRET pairs. *Sensors (Basel)* **16:** 1488. doi:10.3390/s16091488

Börjesson K, Preus S, El-Sagheer AH, Brown T, Albinsson B, Wilhelmsson LM. 2009. Nucleic acid base analog FRET-pair facilitating detailed structural measurements in nucleic acid containing systems. *J Am Chem Soc* **131:** 4288–4293. doi:10.1021/ja806944w

Cawte AD, Unrau PJ, Rueda DS. 2020. Live cell imaging of single RNA molecules with fluorogenic Mango II arrays. *Nat Commun* **11:** 1283. doi:10.1038/s41467-020-14932-7

Clegg RM. 1992. Fluorescence resonance energy transfer and nucleic acids. *Methods Enzymol* **211:** 353–388. doi:10.1016/0076-6879(92)11020-J

Dolgosheina EV, Jeng SC, Panchapakesan SS, Cojocaru R, Chen PS, Wilson PD, Hawkins N, Wiggins PA, Unrau PJ. 2014. RNA mango aptamer-fluorophore: a bright, high-affinity complex for RNA labeling and tracking. *ACS Chem Biol* **9:** 2412–2420. doi:10.1021/cb500499x

Fernandez-Millan P, Autour A, Ennifar E, Westhof E, Ryckelynck M. 2017. Crystal structure and fluorescence properties of the iSpinach aptamer in complex with DFHBI. *RNA* **23:** 1788–1795. doi:10.1261/rna.063008.117

Fessl T, Lilley DM. 2013. Measurement of the change in twist at a helical junction in RNA using the orientation dependence of FRET. *Biophys J* **105:** 2175–2181. doi:10.1016/j.bpj.2013.09.042

Filonov GS, Moon JD, Svensen N, Jaffrey SR. 2014. Broccoli: rapid selection of an RNA mimic of green fluorescent protein by fluorescence-based selection and directed evolution. *J Am Chem Soc* **136:** 16299–16308. doi:10.1021/ja508478x

Franke D, Svergun DI. 2009. *DAMMIF*, a program for rapid *ab-initio* shape determination in small-angle scattering. *J Appl Crystallogr* **42:** 342–346. doi:10.1107/S0021889809000338

Furukawa K, Ramesh A, Zhou Z, Weinberg Z, Vallery T, Winkler WC, Breaker RR. 2015. Bacterial riboswitches cooperatively bind Ni^{2+} or Co^{2+} ions and control expression of heavy metal transporters. *Mol Cell* **57:** 1088–1098. doi:10.1016/j.molcel.2015.02.009

Gohlke C, Murchie AI, Lilley DM, Clegg RM. 1994. Kinking of DNA and RNA helices by bulged nucleotides observed by fluorescence resonance energy transfer. *Proc Natl Acad Sci* **91:** 11660–11664. doi:10.1073/pnas.91.24.11660

Heyduk T. 2002. Measuring protein conformational changes by FRET/LRET. *Curr Opin Biotechnol* **13:** 292–296. doi:10.1016/S0958-1669(02)00332-4

Huang L, Lilley DMJ. 2016. The kink turn, a key architectural element in RNA structure. *J Mol Biol* **428:** 790–801. doi:10.1016/j.jmb.2015.09.026

Iqbal A, Arslan S, Okumus B, Wilson TJ, Giraud G, Norman DG, Ha T, Lilley DM. 2008a. Orientation dependence in fluorescent energy transfer between Cy3 and Cy5 terminally attached to double-stranded nucleic acids. *Proc Natl Acad Sci* **105:** 11176–11181. doi:10.1073/pnas.0801707105

Iqbal A, Wang L, Thompson KC, Lilley DM, Norman DG. 2008b. The structure of cyanine 5 terminally attached to double-stranded DNA: implications for FRET studies. *Biochemistry* **47:** 7857–7862. doi:10.1021/bi800773f

Jeng SCY, Chan HHY, Booy EP, McKenna SA, Unrau PJ. 2016. Fluorophore ligand binding and complex stabilization of the RNA Mango and RNA Spinach aptamers. *RNA* **22:** 1884–1892. doi:10.1261/rna.056226.116

Jepsen MDE, Sparvath SM, Nielsen TB, Langvad AH, Grossi G, Gothelf KV, Andersen ES. 2018. Development of a genetically encodable FRET system using fluorescent RNA aptamers. *Nat Commun* **9:** 18. doi:10.1038/s41467-017-02435-x

Kabsch W. 2010. XDS. *Acta Crystallogr D Biol Crystallogr* **66:** 125–132. doi:10.1107/S0907444909047337

Kashida H, Kurihara A, Kawai H, Asanuma H. 2017. Orientation-dependent FRET system reveals differences in structures and flexibilities of nicked and gapped DNA duplexes. *Nucleic Acids Res* **45:** e105. doi:10.1093/nar/gkx200

Kellenberger CA, Chen C, Whiteley AT, Portnoy DA, Hammond MC. 2015. RNA-based fluorescent biosensors for live cell imaging of second messenger cyclic di-AMP. *J Am Chem Soc* **137:** 6432–6435. doi:10.1021/jacs.5b00275

Kozin M, Svergun D. 2001. Automated matching of high- and low-resolution structural models. *J Appl Crystallogr* **34:** 33–41. doi:10.1107/S0021889800014126

Lacerda R, Menezes J, Romão L. 2017. More than just scanning: the importance of cap-independent mRNA translation initiation for cellular stress response and cancer. *Cell Mol Life Sci* **74:** 1659–1680. doi:10.1007/s00018-016-2428-2

Lakowicz JR, Szmacinski H, Nowaczyk K, Berndt KW, Johnson M. 1992a. Fluorescence lifetime imaging. *Anal Biochem* **202:** 316–330. doi:10.1016/0003-2697(92)90112-K

Lakowicz JR, Szmacinski H, Nowaczyk K, Johnson ML. 1992b. Fluorescence lifetime imaging of free and protein-bound NADH. *Proc Natl Acad Sci* **89:** 1271–1275. doi:10.1073/pnas.89.4.1271

Lau MW, Trachman RJ, Ferré-D'Amaré AR. 2017. A divalent cation-dependent variant of the *glmS* ribozyme with stringent Ca^{2+} selectivity co-opts a preexisting nonspecific metal ion-binding site. *RNA* **23:** 355–364. doi:10.1261/rna.059824.116

Lee W, von Hippel PH, Marcus AH. 2014. Internally labeled Cy3/Cy5 DNA constructs show greatly enhanced photo-stability in single-molecule FRET experiments. *Nucleic Acids Res* **42:** 5967–5977. doi:10.1093/nar/gku199

Lewis FD, Zhang L, Zuo X. 2005. Orientation control of fluorescence resonance energy transfer using DNA as a helical scaffold. *J Am Chem Soc* **127:** 10002–10003. doi:10.1021/ja0524402

McCoy AJ, Grosse-Kunstleve RW, Adams PD, Winn MD, Storoni LC, Read RJ. 2007. Phaser crystallographic software. *J Appl Crystallogr* **40:** 658–674. doi:10.1107/S0021889807021206

Muñoz-Losa A, Curutchet C, Krueger BP, Hartsell LR, Mennucci B. 2009. Fretting about FRET: failure of the ideal dipole approximation. *Biophys J* **96:** 4779–4788. doi:10.1016/j.bpj.2009.03.052

Nahas MK, Wilson TJ, Hohng S, Jarvie K, Lilley DM, Ha T. 2004. Observation of internal cleavage and ligation reactions of a ribozyme. *Nat Struct Mol Biol* **11:** 1107–1113. doi:10.1038/nsmb842

Paige JS, Wu KY, Jaffrey SR. 2011. RNA mimics of green fluorescent protein. *Science* **333:** 642–646. doi:10.1126/science.1207339

Petoukhov MV, Svergun DI. 2007. Analysis of X-ray and neutron scattering from biomacromolecular solutions. *Curr Opin Struct Biol* **17:** 562–571. doi:10.1016/j.sbi.2007.06.009

Rodriguez EA, Campbell RE, Lin JY, Lin MZ, Miyawaki A, Palmer AE, Shu XK, Zhang J, Tsien RY. 2017. The growing and glowing toolbox of fluorescent and photoactive proteins. *Trends Biochem Sci* **42:** 111–129. doi:10.1016/j.tibs.2016.09.010

Sanborn ME, Connolly BK, Gurunathan K, Levitus M. 2007. Fluorescence properties and photophysics of the sulfoindocyanine Cy3 linked covalently to DNA. *J Phys Chem B* **111:** 11064–11074. doi:10.1021/jp072912u

Schmidt A, Gao G, Little SR, Jalihal AP, Walter NG. 2020. Following the messenger: recent innovations in live cell single molecule fluorescence imaging. *Wiley Interdiscip Rev RNA* **11:** e1587. doi:10.1002/wrna.1587

Song WJ, Strack RL, Svensen N, Jaffrey SR. 2014. Plug-and-play fluorophores extend the spectral properties of spinach. *J Am Chem Soc* **136:** 1198–1201. doi:10.1021/ja410819x

Spiriti J, Binder JK, Levitus M, van der Vaart A. 2011. Cy3-DNA stacking interactions strongly depend on the identity of the terminal basepair. *Biophys J* **100:** 1049–1057. doi:10.1016/j.bpj.2011.01.014

Steinmetzger C, Bäuerlein C, Höbartner C. 2020. Supramolecular fluorescence resonance energy transfer in nucleobase-modified fluorogenic RNA aptamers. *Angew Chem Int Ed Engl* **59:** 6760–6764. doi:10.1002/anie.201916707

Strack RL, Disney MD, Jaffrey SR. 2013. A superfolding Spinach2 reveals the dynamic nature of trinucleotide repeat-containing RNA. *Nat Methods* **10:** 1219–1224. doi:10.1038/nmeth.2701

Stryer L, Haugland RP. 1967. Energy transfer: a spectroscopic ruler. *Proc Natl Acad Sci* **58:** 719–726. doi:10.1073/pnas.58.2.719

Suddala KC, Price IR, Dandpat SS, Janeček M, Kührová P, Šponer J, Banáš P, Ke A, Walter NG. 2019. Local-to-global signal transduction at the core of a Mn. *Nat Commun* **10:** 4304. doi:10.1038/s41467-019-12230-5

Svergun D. 1992. Determination of the regularization parameter in indirect-transform methods using perceptual criteria. *J Appl Crystallogr* **25:** 495–503. doi:10.1107/S0021889892001663

Svergun D, Barberato C, Koch M. 1995. CRYSOL—a program to evaluate x-ray solution scattering of biological macromolecules from atomic coordinates. *J Appl Crystallogr* **28:** 768–773. doi:10.1107/S0021889895007047

Tan E, Wilson TJ, Nahas MK, Clegg RM, Lilley DM, Ha T. 2003. A four-way junction accelerates hairpin ribozyme folding via a discrete intermediate. *Proc Natl Acad Sci* **100:** 9308–9313. doi:10.1073/pnas.1233536100

Tolbert BS, Miyazaki Y, Barton S, Kinde B, Starck P, Singh R, Bax A, Case DA, Summers MF. 2010. Major groove width variations in RNA structures determined by NMR and impact of ^{13}C residual chemical shift anisotropy and ^{1}H-^{13}C residual dipolar coupling on refinement. *J Biomol NMR* **47:** 205–219. doi:10.1007/s10858-010-9424-x

Trachman RJ, Draper DE. 2017. Divalent ion competition reveals reorganization of an ion atmsophere upon folding. *Nucleic Acids Res* **45:** 4733–4742.

Trachman RJ, Ferré-D'Amaré AR. 2019. Tracking RNA with light: selection, structure, and design of fluorescence turn-on RNA aptamers. *Q Rev Biophys* **52:** e8. doi:10.1017/S0033583519000064

Trachman RJ, Demeshkina NA, Lau MWL, Panchapakesan SSS, Jeng SCY, Unrau PJ, Ferré-D'Amaré AR. 2017a. Structural basis for high-affinity fluorophore binding and activation by RNA Mango. *Nat Chem Biol* **13:** 807–813. doi:10.1038/nchembio.2392

Trachman RJ, Truong L, Ferré-D'Amaré AR. 2017b. Structural principles of fluorescent RNA aptamers. *Trends Pharmacol Sci* **38:** 928–939. doi:10.1016/j.tips.2017.06.007

Trachman RJ, Abdolahzadeh A, Andreoni A, Cojocaru R, Knutson JR, Ryckelynck M, Unrau PJ, Ferré-D'Amaré AR. 2018. Crystal structures of the Mango-II RNA aptamer reveal heterogeneous fluorophore binding and guide engineering of variants with improved selectivity and brightness. *Biochemistry* **57:** 3544–3548. doi:10.1021/acs.biochem.8b00399

Trachman RJ, Autour A, Jeng SCY, Abdolahzadeh A, Andreoni A, Cojocaru R, Garipov R, Dolgosheina EV, Knutson JR, Ryckelynck M, et al. 2019a. Structure and functional reselection of the Mango-III fluorogenic RNA aptamer. *Nat Chem Biol* **15:** 472–479. doi:10.1038/s41589-019-0267-9

Trachman RJ, Stagno JR, Conrad C, Jones CP, Fischer P, Meents A, Wang YX, Ferré-D'Amaré AR. 2019b. Co-crystal structure of the iMango-III fluorescent RNA aptamer using an X-ray free-electron laser. *Acta Crystallogr F Struct Biol Commun* **75:** 547–551. doi:10.1107/S2053230X19010136

Trachman RJ, Cojocaru R, Wu D, Piszczek G, Ryckelynck M, Unrau PJ, Ferré-D'Amaré AR. 2020. Structure-guided engineering of the homodimeric Mango-IV fluorescence turn-on aptamer yields an RNA FRET pair. *Structure* **28:** 776–785.e3. doi:10.1016/j.str.2020.04.007

Volkov V, Svergun D. 2003. Uniqueness of ab initio shape determination in small-angle scattering. *J Appl Crystallogr* **36:** 860–864. doi:10.1107/S0021889803000268

Warner KD, Chen MC, Song WJ, Strack RL, Thorn A, Jaffrey SR, Ferre-D'Amare AR. 2014. Structural basis for activity of highly efficient RNA mimics of green fluorescent protein. *Nat Struct Mol Biol* **21:** 658–663. doi:10.1038/nsmb.2865

Wu P, Brand L. 1994. Resonance energy transfer: methods and applications. *Anal Biochem* **218:** 1–13. doi:10.1006/abio.1994.1134

Xu J, Cotruvo JA. 2020. The *czcD* (NiCo) riboswitch responds to Iron (II). *Biochemistry* **59:** 1508–1516. doi:10.1021/acs.biochem.0c00074